

# Anisotropic Magnetoresistance (AMR) Magnetometers

Michael J. Haji-Sheikh and Kristen Allen

**Abstract** Anisotropic magnetoresistive (AMR) based magnetometers are used in devices as varied as global positioning systems to provide dead reckoning capability and in automotive ignition systems to provide crankshaft rotational position. Presented are data and methods that can assist in the design and implementation of these systems and a method to design a Helmholtz coil system to test these devices. The transverse and longitudinal behavior of individual AMR sensors along with group (proximity) behavior is addressed with both data and modeling. The design of a 3-axis measurement system goes from basic electromagnetics to the use of COMSOL and the verification of the measurement system using a commercial 3-axis magnetometer.

## 1 Background

When William Thompson (Lord Kelvin) discovered the Anisotropic Magnetoresistance (AMR) effect in 1897 [1] it was but a curiosity of physics. Significant effort through the early part of the Twentieth Century was made in an effort to model and understand this effect. Though, to use AMR to its maximum effect it would take another sixty years of development (including the microelectronics revolution) to make usable thin-films for sensors and memory. In the 1960s, the invention of the integrated circuit along with the space race led to advances in thin film deposition processes that produced high quality magnetic films. The search for a material to be a lightweight non-volatile memory material for space applications, led researchers to develop devices from AMR materials [2] to satisfy these requirements. This memory is called magnetic random access memory or MRAM. Corporations as diverse as IBM, Philips Electronics, TI, and Honeywell have developed variants over the years on this theme. Philips Electronics and

---

M.J. Haji-Sheikh (✉) · K. Allen  
Department of Electrical Engineering, Micro-Electronic Research  
and Development Center, Northern Illinois University, DeKalb, IL 60115, USA  
e-mail: mhsheikh@niu.edu

Honeywell entered the Market in the 1960s, 1970s and into the present day using AMR thin film magnetometers. Over that time period, researchers studied the effect of depositing films under magnetic fields [3, 4] and the sources of noise that would effect low field measurements [5]. Recently, the topic of permalloy deposition in static magnetic fields has become of interest again as shown in this recent paper by García-Arribas et al. [6]. Commercial uses of AMR magnetometers consist of high current detection (overload current detection in power distribution), position sensing, tachometry, low magnetic field anomaly detection, and multi-axis compasses.

## 2 Physical Model

Magnetoresistance can be broken into two types, ordinary and anisotropic. Ordinary magnetoresistance is often exhibited by non-magnetic metal and semiconductors. The effect is due to the shorting out of the Hall voltage which then increases the path length of the electrons which in turn increases the resistance. The ordinary magnetoresistance equation is

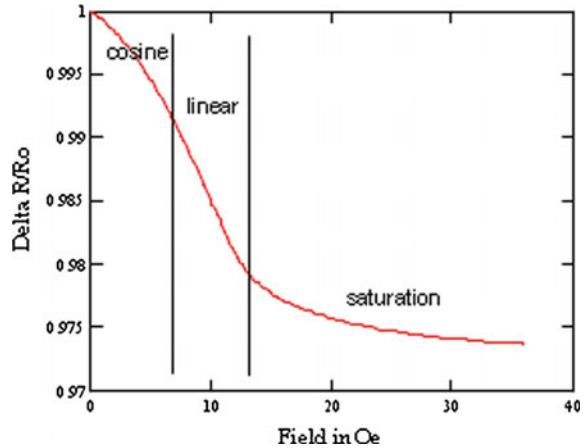
$$\frac{\Delta\rho}{\rho_0} = C \cdot \mu \cdot B^2 \quad (1)$$

where  $C$  is a constant,  $\mu$  is the mobility, and  $B$  is the normal magnetic field. This effect is mostly used in indium antimonide magnetoresistors produced by Asahi Chemical Industry. The InSb compound semiconductor can have extremely high mobilities (60,000–80,000 cm<sup>2</sup>/V s). During the late 1980s and early 1990s GM research advocated the use of InSb sensors in crank-sensor applications [7] and deployed some of these sensors in vehicles such as their Cadillac luxury line.

Automotive AMR sensors come in two types: High-field sensors that sense primarily angle; Low-field that sense magnitude. The range of what is considered high field depends on the application. A high field sensor for an AMR device is an in-plane field level that is high enough to keep the sensor in saturation. It is common to discuss field levels in magnetic sensors in units of Oersteds or Oe since a Tesla is quite a large unit for normal uses. For many AMR sensors this corresponds to greater than 25–30 Oe. A low-field sensor operates below the onset of saturation. Figure 1 shows the response of a single AMR resistor element. The lower region behaves in somewhat a sinusoidal manner while the next region is somewhat linear and the last region is the saturation region. This curve is often described as  $\cos^2$  behavior

$$\frac{\Delta R}{R_0} = \Delta R_{max} \cos^2 \theta. \quad (2)$$

**Fig. 1** The transverse magnetoresistance curve for a 37.5 nm and 35  $\mu\text{m}$  wide resistor. This field response curve is entirely dependent on geometry of the sensor (width and thickness)



A solid monograph on the design of AMR sensors, as defined through the 1990s and published in 2001 is authored by Tumanski [8]. Tumanski defines a broader set of application devices and analyzes some giant magnetoresistive (GMR) devices where this article only will consider AMR devices. Tumanski outlines much of the design criteria for various magnetic sensors and is a pioneer in the use of AMR sensors for many commercial applications.

## 2.1 Theoretical Behavior

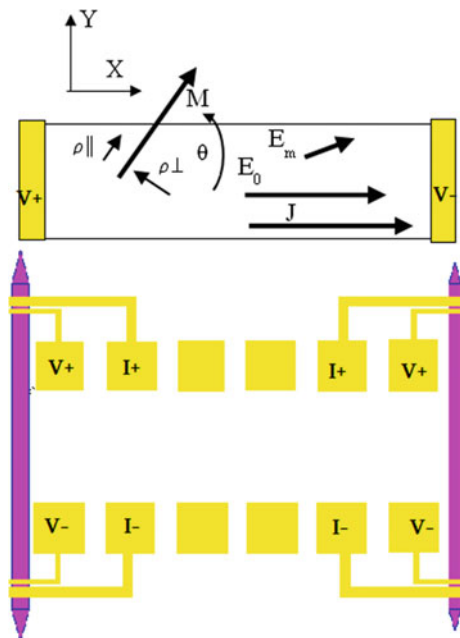
The ordinary magneto-resistance effect is present in all metals and was first observed by Hall [9] in his groundbreaking paper on “A New Action of the Magnet on Electric Currents” in 1879 then followed by William Thompson’s discovery of the AMR effect in 1897. After almost of a century of work by various researchers such as Birss [10] and Stoner and Wolforth [11], the material went from a curiosity to a commercial success in transformer cores, to modern magnetic sensors and magnetic memory. The theoretical models can date back to the research work done by the people at IBM’s Watson Research Center [2, 12]. A physical model put forth [2] is the increase in resistance due to s-d interband scattering. Magnetoresistance can be broken into two types, ordinary and anisotropic. Additionally Batterel and Galinier [13] pointed out a novel effect that appears in AMR materials, this effect is described as the planer hall effect and come out of the tensor analysis of the AMR effect. This effect is often used in MRAM (magnetic random access memory) not generally used in magnetometry. The anisotropy constant can be determined by the planer hall effect according to Chang [14].

## 2.2 The Resistivity Tensor

A physical model for the behavior of an AMR sensor is a necessary step to allow these sensors to be used in design. Most models start with trying to fit data and theory to a resistor below the saturation point. As we were designing sensors for various saturation mode applications, it was painfully obvious that that method was not applicable to the situation presented. Testing shows that rotating a saturating field created a very well defined sinusoidal behavior. This did not match the  $\cos^2\theta$  behavior outlined in a plurality of journal papers. For us to use an equation in our modeling at the time, we needed to rethink this equation. An experiment to develop this physical model was devised at the time that would incorporate everything we knew about measuring resistors. Figure 2 shows the basic resistor design used to develop a Maxwell's equations based model to characterize the behavior of saturated elements. The basic concept is to use Kelvin connected resistors that have a well defined current launching structure that will behave in a manner which can make extracting behavior a simple mathematical exercise. A common measurement technique for these films has been to use a Vander Pauw structure. The Vander Pauw structure is not useful for these type of magnetic tests due to the current never following a straight line in one of these structures.

Figure 3 is a graph of the data generated for a group of magnetoresistive elements tested in the saturation region [15].

**Fig. 2** CAD layout of a typical AMR thin film Kelvin resistor along with a schematic of the vectors present in the given device. *This image is care of Honeywell's Sensing and Control Division*



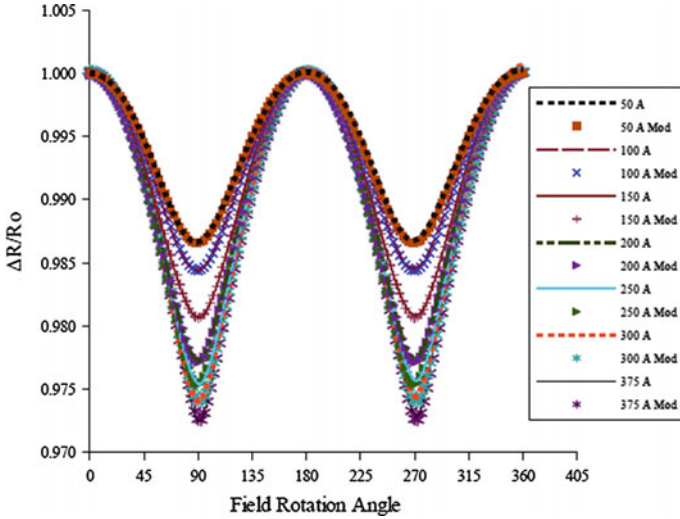


**Fig. 3** Saturated magnetoresistors tested through 360°. The data is from Haji-Sheikh et al. [15]. This graph also includes the results of modeling

The sensor model behavior is the result of solving a 2d tensor that starts by assuming isotropic and anisotropic behavior for a magnetoresistor. The error often made in this solution is the dropping of one of the current elements that relates to the transverse current in a resistor. The full tensor to solve for the saturated magnetoresistance is as follows

$$P'_{total} = \begin{bmatrix} \rho_0 & 0 \\ 0 & \rho_0 \end{bmatrix} + \begin{bmatrix} \rho' + \Delta\rho' \cos(2\theta) & \Delta\rho' \sin(2\theta) \\ \Delta\rho' \sin(2\theta) & \rho' - \Delta\rho' \cos(2\theta) \end{bmatrix} \quad (3)$$

By solving the following relationship,

$$\vec{E} = \rho \vec{J} \quad (4)$$

where  $E$  is the electric field and  $J$  is the current density. The modified AMR relationship can be shown to be similar to the Mohr’s circle as described in Nye [16] and is as shown in equation,

$$\rho_{eff} = \rho_0 + \rho' \sqrt{\left(1 + \frac{\Delta\rho'}{\rho'} \cos(2\theta)\right)^2 + \left(\frac{\Delta\rho'}{\rho'} \sin(2\theta)\right)^2} \quad (5)$$

with the only difference from a mechanical system is the lack of off-axis shear components. So that the measured resistance is

**Table 1** Coefficients of fit for permalloy magnetoresistors

	Film thickness						
	5.0 nm	10.0 nm	15.0 nm	20.0 nm	25.0 nm	30.0 nm	37.5 nm
A	0.97923	0.97580	0.97340	0.97090	0.97050	0.96968	0.97000
B	0.01420	0.01640	0.01695	0.01695	0.01726	0.01722	0.01630
C	0.480	0.480	0.572	0.572	0.718	0.769	0.845

$$V = \rho_{\text{eff}} \frac{\text{length}}{\text{area}} \cdot I \quad \text{or} \quad (6)$$

$$V_{\text{total}} = I_s R_0 \left[ A + B \sqrt{(1 + C \cos(2\theta))^2 + (C \sin(2\theta))^2} \right]$$

The value of  $R_0$  is also experimentally determined since it represents the resistance with no applied field (Table 1).

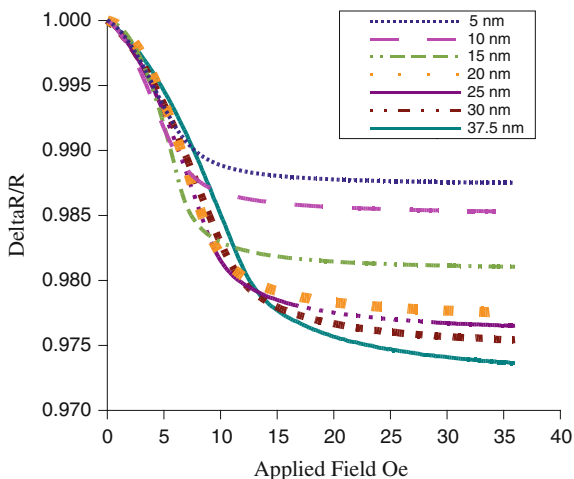
These empirical results allow for a high precision fit to the permalloy and are consistent with Maxwell's equations. For a sensor below saturation the modeling is not so simple. Many things influence the results including the proximity of the other sensor elements, length, width, and thickness. Some automotive designs operate between 0.1 and 0.2 T (1000–2000 G) which is far above the sensor saturation level. Above saturation, proximity and geometry don't have much of an effect but below saturation these effects become designable parameters and can have a significant effect on the overall results.

### 2.3 Cross Axis Behavior Unsaturated Single Resistor Element

The range of what is considered high field changes from sensor to sensor design. A high field sensor for an AMR sensor is an in-plane field level that is high enough to keep the sensor in saturation. It is common to discuss field levels in magnetic sensors in units of Oersteds or Oe (Gauss in air). For many AMR sensors this corresponds to greater than 15–30 Oe. A low-field sensor operates below the onset of saturation. Figure 4 shows the response of a single AMR element with different thicknesses. This behavior is representative of the rotation of micro-magnetic domains. These domains will rotate until they reach a maximum angle which will be a number somewhat lower than ninety degrees.

The below saturation mode in automotive sensing is not as common as the above saturation mode sensors but it does show up in current sensing in electric vehicles and in sensing the Earth's magnetic field. The high-current sensors are generally designed as meander sensors but have to take in account the design parameters not needed for the above saturation devices. Figure 5 shows various representations of the magnetization and behaviors of the sensors below saturation.

**Fig. 4** Transverse magnetoresistance curves from a 5 to 37.5 nm thick 35 μm wide resistor. The saturation region of this curve is controlled by geometry. Thinner films have a lower saturation field and a lower maximum change in resistance



The Stoner-Wohlfarth model is often used to represent the behavior of magnetoresistors within the full range of hysteresis, as shown in Fig. 5. To approach magnetization rotation, we can look at minimizing the energy of the magnetic system so from Chikazumi and Charap [17] we get,

$$E = -K_u \cos^2(\theta - \theta_0) - M_s H \cos \theta \tag{7}$$

where  $M_s$  is the saturation magnetization,  $H$  is the external field,  $\theta$  is the angle between  $H$  and  $M_s$  and  $\theta_0$  is the angle between  $H$  and the easy axis (EA). The anisotropy constant  $K_u$  acts like the spring constant for a rotating spring and is the energy that it takes to return the magnetization back to the original position. It is important to characterize the permalloy out of any particular deposition process since no two deposition systems will produce identical material. The two main numbers that are needed to be compared from machine to machine are the values of  $H_c$  and  $H_k$ . The  $H_c$  value represents the easy-axis hysteresis and the  $H_k$  represents the hard-axis slope between the saturation levels. There are commercial B-H

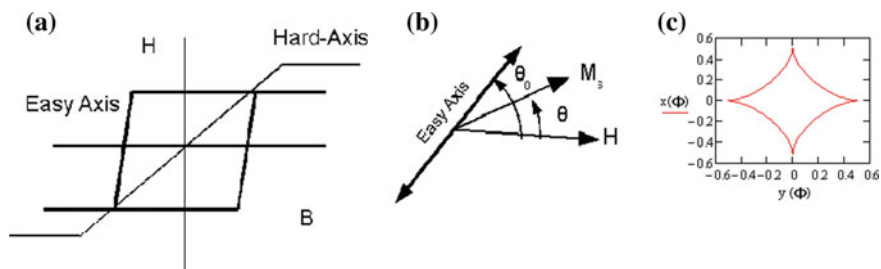
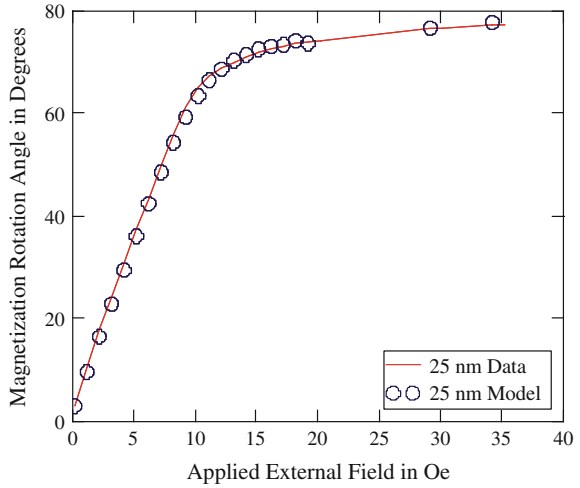


**Fig. 5** a The B-H behavior of an ideal thin film. b A magnetic free body diagram representing the thin-film resistor. c A plot of the Stoner-Wohlfarth asteroide is shown

**Fig. 6** The angle  $\theta$  versus applied external field  $H$ . Also shown is the results of attempting to create a model to fit the rotation of the magnetization with  $H$ . There is significantly more transition than the S-W predicts



looping systems that will measure these values inductively directly on a deposited substrate. That means that Eq. (8) needs to be matched to an actual test structure. To extract  $\theta$  for a given design, the following equation can be used to extract the angle

$$|\cos \theta| = \sqrt{\frac{1}{4C} \left[ \left( \left( \frac{V_0}{I_S R_0} - A \right) \frac{1}{B} \right)^2 - C^2 - 1 + 2C \right]} \quad (8)$$

where the values of  $A$ ,  $B$ , and  $C$  come from Eqs. (8) and (9). The angle  $\theta$  can be plotted against applied  $\theta$ . A graph of this is shown in Fig. 6 for a 25 nm. Equation (12) is a first attempt to model the behavior using a magnitude tensor ratio

$$\Delta\theta = \frac{M}{2K_u} H = \frac{M_0 \sqrt{(1 + \alpha \cos 2\theta)^2 + (\alpha \sin 2\theta)}}{2K_u \sqrt{(1 + \delta \cos 2\theta)^2 + (\delta \sin 2\theta)}} \quad (9)$$

where  $M_o$  is considered to vary rhombohedrally and  $K_u$  is also varying in the same fashion. The values for  $\delta$  and for  $\alpha$  are also experimentally determined and the equation is solved transcendently.

The model can then be substituted into Eq. (4) and compared to the original data. The initial data and experiments indicates that this model can fit actual data. The relationships then can create a conceptual basis for a more complete model in the future.

It is important to reinsert the rotation data (Fig. 7) into the model to determine if the magnetization rotation model works. This is to match the modeled data to the



**Fig. 7** Rotation angle for resistors of the same width and different thicknesses. It is clear that the thicknesses change the maximum rotation angle. The maximum angle of rotation appears to be actually lower for the thinner resistors. Width equals 35  $\mu\text{m}$

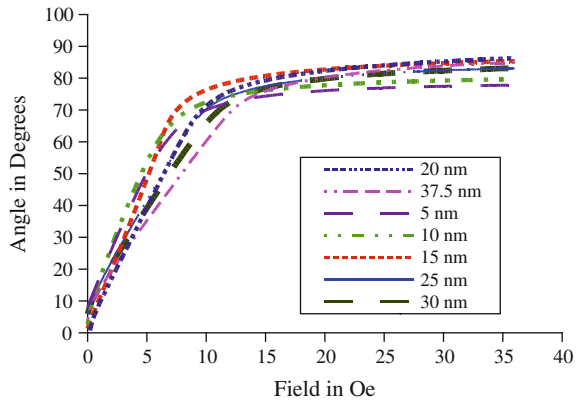
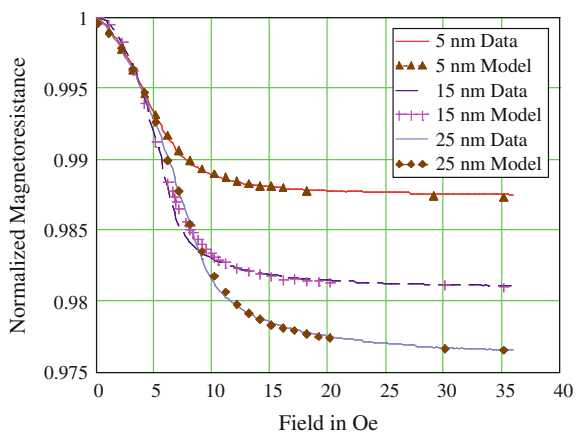


**Fig. 8** This is a graph of magnetic response of single resistors of constant width but varying thickness. This graph demonstrates the behavior of the model versus the actual sensor results. Unfortunately the model is not as predictive as necessary, but it does show the relationship between the earlier saturation model and the below saturation behavior

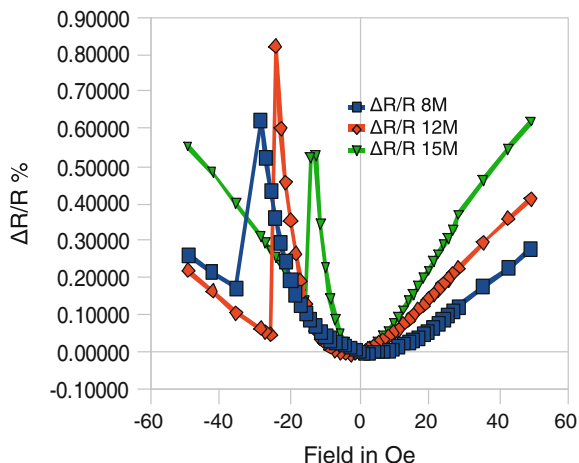


original data. The result for this comparison is shown in Fig. 8. Normally this data is fitted using a piecewise model as shown in Tumanski [8] but this new approach allows the model to be appear contiguous.

### 2.4 Longitudinal Axis Behavior Unsaturated Single Resistor Element

An important sensor response that needs to be understood is the off-axis behavior. This off-axis behavior is most interesting when looking at a 45° field to the current direction and then when the field is rotated 180° from the magnetization direction. The resistors force the magnetization to line up with the resistor direction and without an applied external field the magnetization and the current is parallel to the current direction. With these responses, hysteresis is defined. This is specific to a below saturation element and

**Fig. 9** 45° off-axis behavior for three different widths of a resistor with the same thickness. The results up until the switching field show a behavior (as they should) similar to a barber-pole sensor



often a source of error. The schematic in Fig. 5 shows an ideal hysteresis behavior and we can compare this with Fig. 9 which shows the 45° off-axis applied field behavior. The first quadrant applied field is in the direction in which the magnetization is set (right side) and the third quadrant applied field is in the opposite direction of the set magnetization (left side). This displays two effects need to produce a compass chip. One of these effects is the asymmetry of the resistor response and the other is the hysteresis caused by the reversal of the magnetization.

The hysteresis effect that is often observed in certain sensors can be demonstrated by applying the field at forty-five degrees to the resistor. Each measurement point is around a milligauss so that the domain reversal happens in a narrow field range. To demonstrate the reversal effect at its strongest, a group of individual resistors were bias longitudinally. These resistors were on four wafers to reduce the effect of manufacturing variability on the experiment. There was no attempt to reproduce this data with the effect of proximity on this set of samples. According to Tanaka, Yazawa and Masuya [18], in their study of magnetization reversal in cobalt thin films, the magnetization reversal is always preceded by a non-coherent rotation process and is heavily influenced by crystalline grain orientation. During the processing of permalloy films often multiple layers are deposited to build up the target thickness. The single layer films have Bloch wall displacement where multilayer devices have Neel wall displacement [19]. This multilayer structure lowers the switching field. The films in the following graphs have multiple layers (2 minimum and 10 maximum). They exhibit switching fields that are strongly affected by the thickness of the films and by the width of the patterned resistors. The results in Fig. 9 demonstrate the behavior of a single resistor element being biased by an external magnetic field at forty-five degrees. As expected, the resistor behaves much as a barber-pole sensor behaves until the switching field is reached. When the magnetization reversal occurs, the resistance change mirror images the right half plain behavior.

**Fig. 10** Resistance of individual resistors biased magnetically along the current direction. The resistor thickness is 25 nm and all resistors are the same length

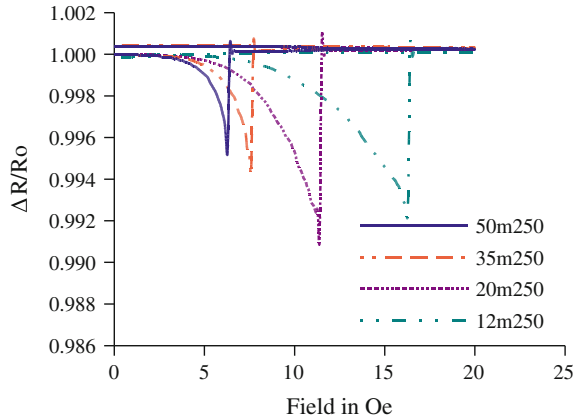
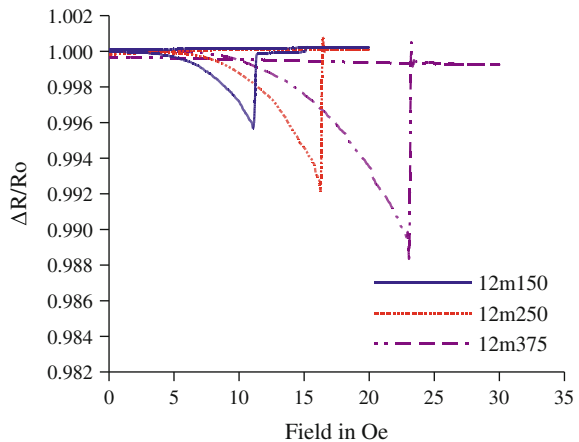


**Fig. 11** Resistance of individual resistors biased magnetically along the current direction. The resistor thickness varies from 15, 25, 37.5 nm and the width is 12  $\mu\text{m}$  and all resistors are the same length



The next set of graphs show the results of using an external bias field along the resistor direction and in the opposite direction of the magnetization for that resistor. Figures 10, 11, 12, 13 and 14 demonstrate the effect of patterning and film thickness on the reversal field for an 81 % Ni/19 % Fe permalloy film. It is clear that the switching field drops with patterned resistor width. In Fig. 10, the film thickness was 25 nm (250 Å) and the resistors appear to go through a single reversal point which would indicate that there is a certain amount of coherency in this behavior. In Fig. 11 the comparison is with a constant resistor width (12  $\mu\text{m}$ ) and varying the thickness from 15, 25, and 37.5 nm. This shows that the switching field is increasing with increasing film thickness. This is consistent with the increasing magnetic material volume.

The effects of using a very narrow resistor i.e. 6  $\mu\text{m}$  as patterned, is shown in Fig. 12 while Figs. 13 and 14 show 15 and 20  $\mu\text{m}$  resistors. Several things come out of these figures. The effect of edge in support of the magnetization reversal is

**Fig. 12** Resistance of individual resistors biased magnetically along the current direction. The resistor thickness varies from 15, 25, 37.5 nm and the width is 6  $\mu\text{m}$  and all resistors are the same length

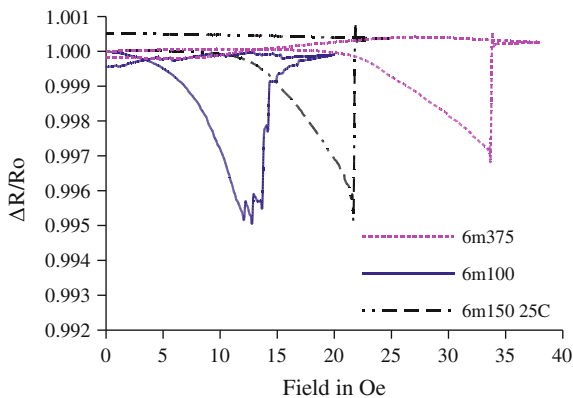


**Fig. 13** Resistance of individual resistors biased magnetically along the current direction. The resistor thickness varies from 10, 15, 25, 37.5 nm and the width is 15  $\mu\text{m}$  and all resistors are the same length. The domain reversal is not as sharp at 10 nm

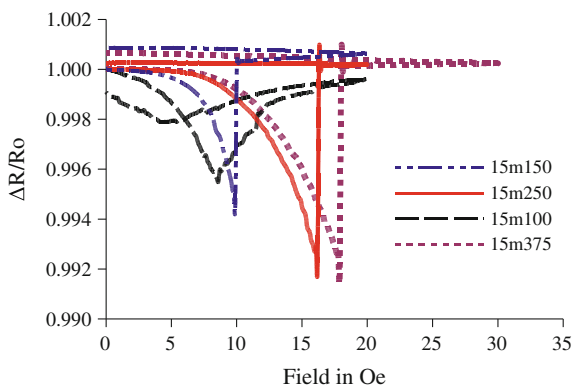


**Fig. 14** Resistance of individual resistors biased magnetically along the current direction. The resistor thickness varies from 10, 15, 25, 37.5 nm and the width is 20  $\mu\text{m}$  and all resistors are the same length. The domain reversal is not as sharp at 10 nm

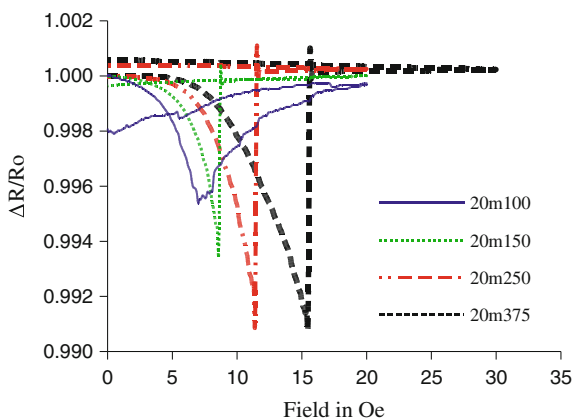
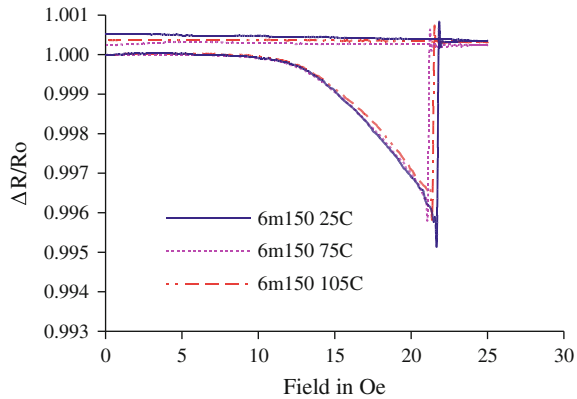


**Fig. 15** Resistance of an individual resistor biased magnetically along the current direction. The resistor thickness is 15 nm and the width is 6  $\mu\text{m}$ . This experiment was performed at 3 different temperatures and shows the magnetization reversal is relatively independent of temperature

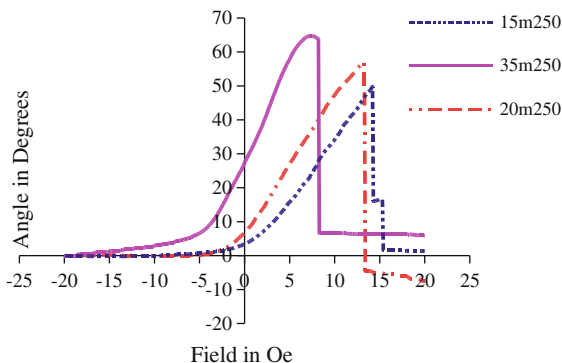


quite strong. As the resistor gets narrower the field required to reverse the magnetization gets higher. This is consistent with present design philosophy and theory. The thickness also has an effect on the reversal of the magnetization. Not only does the thinner sensors demonstrate lower magnetization reversal, the thinnest sensors (10 nm) show significant anisotropy dispersion. This dispersion is not evident in the thicker resistors. Also, this dispersion effect is also interactive with the support from the edge effect. This is also demonstrated with the 10 nm sample which, when the resistor was patterned at 6  $\mu\text{m}$ , the apparent dispersion was reduced and the reversal point was increased. This dispersion effect, in the range of the test, does not seem to be as strong as the thickness to width ratio from 15 nm and up. Additional measurement in this range could support a strong micro-domain numerical model.

Another question that was attempted to be answered by this experiment was whether or not temperature, in a narrow range, has an effect on the reversal value. Figure 15 shows the resistance of an individual resistor biased magnetically along the current direction. The resistor thickness is 15 nm and the width is 6  $\mu\text{m}$ . This resistor was chosen because of the strong magnetization reversal value above 20 Oe. This experiment was performed at 3 different temperatures and shows the magnetization reversal is relatively independent of temperature in that narrow range.

The magnetization rotation angle was calculated for the resistors going through domain reversal. This calculation is shown in Fig. 16 and demonstrates that the magnetization rotates somewhere between 50° and 65° of rotation prior to reversing direction. Interestingly enough, the 35  $\mu\text{m}$  resistor shows a result that implies that some portion of the resistor is rotating past 90° since the resistance is starting to decrease smoothly prior to reversal.

**Fig. 16** Calculated angles for longitudinally biased resistors using Eq. (11) to determine the edge effect. The three resistors were next to each other on the same silicon substrate. The magnetization reversal occurs between  $50^\circ$  and  $65^\circ$  of rotation prior to reversing direction



## 2.5 Cross Axis Behavior for the Unsaturated Barber-Pole

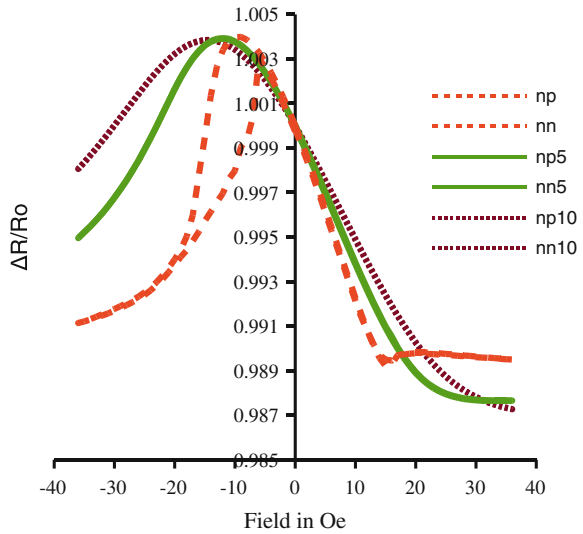
Since the resistance change is coupled to the current direction, a different type of sensor was developed. Commercial entities such as Philips and Honeywell have produced compass chips using a design called the barber-pole. Unlike the previous structures, the barber-pole steers the current  $45^\circ$  to resistor direction. This allows the maximum field to be  $90^\circ$  to the resistor direction and improves magnetization control. One of the primary uses of an AMR sensor is for a below saturation direction sensor. The normal behavior of an AMR resistor can be characterized as an even function sensor i.e. symmetrical about “y” axis. The resistance of these barber-pole structures in a ninety degree applied field is shown in Fig. 17.

Figure 18 is a single element barber-pole resistor. The resistor is  $35 \mu\text{m}$  in width and has  $45^\circ$  shorting straps. The np in the graph means we are setting the magnetization in the negative direction and sweeping the field in the positive direction, and the nn means that we are setting the field in the negative direction and sweeping the field in the negative direction. These samples had a fixed offset field i.e. bias field of 0, 5, and 10 Oe. The classic compass chip behavior is obtained by summing resistor values that have different shorting  $+45^\circ$  (and + current) shorting bars and  $-45^\circ$  (and -current) to linearize the main sensing region. The resistance of these structures is inverse to the desired behavior, the wider structures have lower resistances which in turns says that the larger the resistor bridge the better the compass, but in general a more expensive part. These resistors are sensitive to magnetization reversals so that it is important to have a calibration routine that includes a magnetization reset function. A barber-pole sensor when placed in a

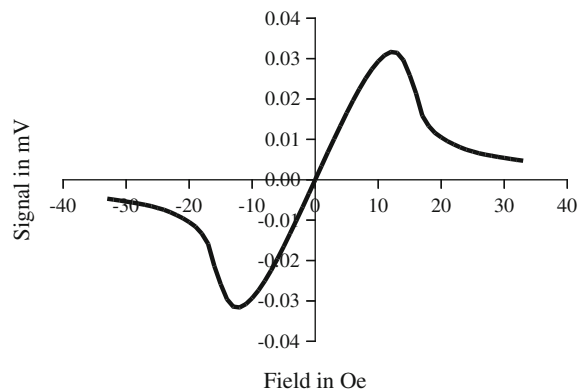
**Fig. 17** Barber-pole sensor element, aluminum shorting straps for redirecting the current



**Fig. 18** Single element barber-pole resistor. The resistor is 35  $\mu\text{m}$  in width and has 45° shorting straps. The np means, negative set field/positive sweep, and nn means negative set field/negative sweep. No number means no longitudinal bias while the 5 means 5 Oe and the 10 means 10 Oe



**Fig. 19** Bridge response calculated for a 4 resistor array with no proximity effect. The proximity effect will increase the sensitivity of the sensor by as much as a factor of 5



saturation field behaves similar to a non-barber pole sensor except that the phase is shifted by forty-five degrees.

Figure 19 shows a bridge response calculated from a 4 resistor Wheatstone bridge with no proximity effect. The proximity effect will be shown in the next section. The source resistor data comes from the resistor in Fig. 18. The proximity effect will increase the sensitivity of the sensor by as much as a factor of 5. The advantage of a barber-pole magnetometer is that you get a very sensitive resistor along with high linearity and good directional sense. Unfortunately these sensors need either a magnet to support a consistent magnetization direction or some form of set-reset circuitry and corresponding structures.

### 2.6 Proximity Effect

The proximity effect, in AMR sensors, is unique in sensing. Anisotropic magnetoresistors change sensitivity when placed in close proximity of each other, which is quite unlike any other sensors. Two pressure sensors next to each other do not change their sensitivity, two flow sensing elements cannot either. This effect is caused by the coupling of each sensing element magnetically. A good demonstration of this effect can be visually demonstrated by using inexpensive compasses and placing them in close proximity of each other. Each compass starts effecting the previous compass till all the compasses have more effect on each other then the Earth’s magnetic field has on the compasses. Figure 20 is a schematic of a resistor array used to demonstrate the effect of proximity.

So in the sensor element, as the space between each element get closer, the effective transverse sensitivity increases. The proximity effect has been modeled by B.B. Pant [20] and is as follows,

$$\alpha(r) = 2 \cdot \left( \frac{r}{(1 + 2 \cdot r)} \right) + \left( \frac{r}{(2 \cdot (1 + r)^2)} \right) \cdot \left( \frac{\pi^2}{2} - 4 \right) \tag{10}$$

where  $\alpha(r)$  is the geometric correction factor based on the distance  $r$  that is the resistor separation distance. This factor is then used as a correction factor for the demagnetization factor,

$$G(r, t, w) = \frac{t}{w} \cdot \alpha(r) \tag{11}$$

The demagnetization factor  $G(r, t, w)$  is now a function of the gap ( $\alpha(r)$ ), the thickness  $t$ , and the resistor width  $w$ . Table 2 shows how a this factor can be used to find equivalent thickness, width, and gaps for designing in proximity. These values are quite reasonable. Figure 21 demonstrates the demagnetization factor  $G(r, t, w)$  by holding the gap to 6  $\mu\text{m}$  and varying the resistor width from 12 to 35  $\mu\text{m}$ . These results show a significant sensitivity difference between the elements. The sensitivity is usually represented by

**Fig. 20** Multiple resistor strip model for proximity effects

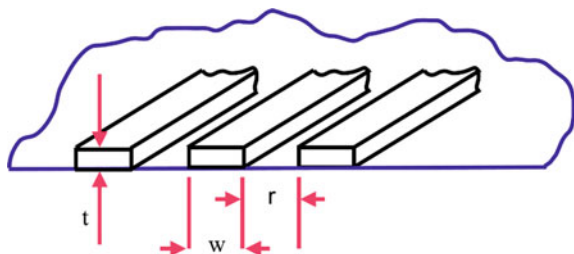
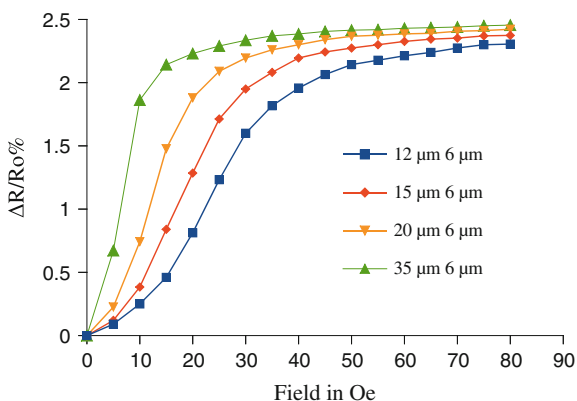




**Table 2** Geometric correction factors for 2 different bridge designs

	Gap $\mu\text{m}$	$\alpha$ (r)	t ( $\mu\text{m}$ )	w ( $\mu\text{m}$ )	G (r, t, w)
r1	6	0.9803	0.035	20	0.00170
r2	3	0.9448	0.020	11	0.00172

**Fig. 21** The demagnetization factor  $G(r, t, w)$  effect demonstrated by holding the gap to  $6 \mu\text{m}$  and varying the resistor width from 12 to  $35 \mu\text{m}$



$$S = \frac{dR}{R_0 dB} \tag{12}$$

where  $R$  is the resistance at the starting point in the field range of interest,  $dR$  is the change in the resistance, and the  $dB$  is change in the magnetic flux. Unfortunately, proximity does not effect resistors being biased longitudinally, which does effect the usefulness of the proximity effect in  $0^\circ-90^\circ$  Wheatstone bridge configured sensors. Narrow resistors as shown Figs. 10, 11, 12, 13 and 14 have reversal values much higher than the wider resistors therefore producing a much larger hysteresis loop, but a better low field sensor (less than 10 Oe). Wider resistors produce a much better medium field range sensor i.e. greater than 11 Oe but lower than saturation since the hysteresis is usually less than 10 Oe.

### 3 Noise Sources and Behavior

Noise sources and the behavior of permalloy thin films at dc to high frequency have been studied since these materials have been used for magnetic recording heads. There are multiple reasons for noise in AMR materials but the most common source is Barkhausen noise. Baldwin and Pickles [19] in 1971 experimented with thin permalloy films to determine what model that the Barkhausen noise behaves like. The term Barkhausen noise often refers to the erratic pops that are often heard in older sound systems which use soft-magnetic materials. In the analysis above, the

flux applied to the test samples were varied linearly over time. The conclusions for this was to determine that the Barkhausen noise in the materials analyzed were due to statistical fluctuations. For an exponential distribution function i.e. the power spectrum  $G_p$  the concept that was put forward to analyze the effect with a breakable spring model,

$$f(z, z_0) = kz_0 \leq z \leq z_0 \quad (13)$$

$$f(z, z_0) = 0z \leq 0, z \geq z_0 \quad (14)$$

and the exponential distribution function,

$$z_0 n(z_0) = N \exp(-z_0/Z) \quad (15)$$

then by integrating,

$$G_p(b) = (1/A_u) \int_{-\infty}^0 dz_0 n(z_0) \left[ \int_{L_p} \exp(-j p z) f(z, z_0) dz \right]^2 - \left[ \int_{L_p} dz \int_0^{\infty} dz_0 n(z_0) f(z, z_0) \right]^2 \delta(p) \quad (16)$$

we get

$$\frac{G_p(p)}{P_c^2} = \frac{4}{NA_u} \frac{1}{(pZ)^{-1}} \left( \left( (pZ)^2 \frac{(pZ)^2 - 1}{(pZ)^2 + 1} \right) + \ln[(pZ)^2 + 1] \right) + \delta(p) \quad (17)$$

and the coercive pressure is,

$$P_c = \frac{1}{2} NkZ^2 \quad (18)$$

$N$  and  $Z$  are density and length parameters,  $L_e$  is the length of the wall travel perpendicular to the wall,  $z_0$  is the defect range,  $A_u$  is the are of the domain wall  $p$  is the spatial frequency.

Shape anisotropy and defects have an effect on higher frequency behavior, this was demonstrated by Grimes et al. [21]. They experimented on thin permalloy films by patterning repeated arrays of holes in the film. This showed that a variation of thicknesses and hole patterning created compensating demagnetization factors. Another form of error is hysteresis caused by the formation and annihilation of edge walls in the sensor elements. This was demonstrated by Mattheis et al. [22] by using high fields perpendicular to the resistor. The edge walls were observed using Kerr microscopy. Additionally, the pinning mechanism at the edge walls was observed

by seeing cross-tie walls on thin permalloy films using scanning electron microscopy with polarization analysis was used to image the surface magnetic domain structure after exposure of the permalloy film to an ac field as shown by Lee et al. [5]. Recently, Zhang et al. [23] have demonstrated Y-factor noise measurements for sub-micron permalloy arrays. Their test setup was configured using co-planer waveguides and patterned permalloy. The noise figures were extracted from the following equation

$$F = \frac{N_a + kT_0G_s}{kT_0G_s} \quad (19)$$

where  $F$  is the noise figure,  $k$  is Boltzmann's constant,  $G_s$  is the system power gain,  $N_a$  is the added system noise, and  $T_0$  is 290 K. The noise voltage density for the permalloy array will vary with bias voltage and will produce various ferromagnetic resonance peaks. The noise, from the measurements, is Johnson-Nyquist noise which comes from the real part of an RLCG model. The noise voltage density for this array approach is

$$V_N = 4NkT\Delta R \quad (20)$$

where  $N$  is the total number of array elements and  $\Delta R + R$  is the output of the measurement system. The measurements in this analysis show even low noise voltage density for frequency measurements in the 2–10 GHz frequency range. This was less than 1 nV<sup>2</sup>/Hz except at resonance where it was 2 nV<sup>2</sup>/Hz at resonance which is quite low.

## 4 Fabrication Methods

Over the years, various physical deposition methods have been used as techniques to create sensing films. These methods include e-beam evaporation, filament evaporation, ion beam deposition and sputter deposition. The sputter deposition methods include DC (Direct Current), DC-magnetron, RF (radio-Frequency), and RF magnetron plasma deposition. The most effective method used to manufacture the AMR sensors is a combination of radio frequency magnetron plasma deposition and strong enough magnets to bias the film during deposition. This allows the film to be deposited incorporating the minimum in trapped gases since the plasma can run in a pressure as low as 1 mTorr. Plasma deposited films will trap gasses as shown in van Hattum et al. [24] who shows that the argon incorporation can be as high as four percent in the film. Early deposition experiments using rf-plasma showed that this gas incorporation can create delaminations of the film. The stresses from these trapped gases can effect the maximum magnetoresistive change and stability of the sensor. Another important variable to control during the deposition phase is the system base pressure. Base pressure in the 10<sup>-8</sup> Torr range will

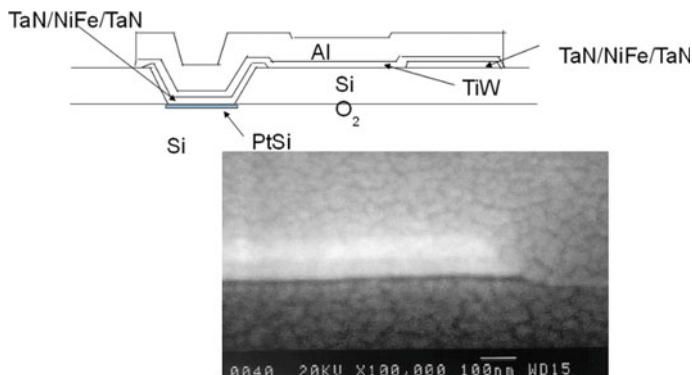


**Fig. 22** Monolithic AMR sensor element. The total element is around 1500 nm thick. *From the Author*

minimize oxygen incorporation in the film. When creating a sensor film it is important to protect the permalloy (AMR sensor film) as much as possible from oxidation. Iron and nickel oxides will reduce the range of the sensor and create a much higher  $H_c$  which will increase the stiffness of the film. Many process chemicals will attack the permalloy film if it is left unprotected. The relatively high iron contact makes the film rather sensitive to chlorine compounds. To prevent these problems from happening, many people use a thin protective coating of tantalum nitride. The film then can be handled like any other metallic film and patterned with photoresist without the worry of contamination. A dry etch is recommended at this point since the protective films are usually wet etch resistant and most wet permalloy etches are inconsistent at best. The most common way of etching permalloy is to use a neutral beam ion-mill [15]. Figure 22 shows a schematic of a scanning electron microscope image of an AMR sensor element on a monolithic device. The sensing film, TaN/NiFe/TaN, is deposited on an integrated circuit with the semiconductor contacts open. The film is then coated with positive acting photoresist and exposed through a patterned photomask. All areas with semiconductor contacts are covered with resist and also the pattern for the sensor is covered with the resist.

After the ion-milling process and after the photoresist is removed, every contact will be covered with a residual stack of material. The advantage of this is that this residual material acts as an electromigration barrier for the contact also. The TiW/Al wiring layer is deposited on the surface and patterned and then the entire wafer is coated with silicon nitride. To reduce process stresses, the assembly is annealed in forming gas for at least 30 min at temperatures greater than 400 °C. This step will lower the resistance of the permalloy and maximize the magnetoresistance. To analyze the effects of the thickness on crystallography, several different samples were sent to Argonne National Labs advanced photon source. The results show that as the NiFe thickness increases the face centered cubic [111] becomes enhanced [25]. This enhancement can explain the change in film behavior in films less than 10 nm in thickness.

## 5 Using a Magnetometer to Calibrate a 3 Axis Helmholtz System

To demonstrate the one application of an AMR magnetometer, a 3 axis Helmholtz low field system was chosen. To evaluate a sensor design the magnitude and direction of the generated magnetic fields must be known or easily determined. Since the magnetometers to be tested are capable of measuring the surrounding magnetic fields along the  $x$ ,  $y$ , and  $z$  axes, the system must be able to generate magnetic fields in these three directions simultaneously. These design requirements are fulfilled by the proposed arrangement of three pairs of Helmholtz Coils placed along the three orthogonal directions. A pair of Helmholtz Coils is separated by the value of their shared radius. However, when there are three sets of coils all with the same coil radius and separated by that same coil radius along the  $x$ ,  $y$ , and  $z$  directions, an intersection would need to occur between these coils. Therefore, in the system ultimately derived and laid out below, the three pairs are separated by their diameter. This structure will be referred to as a modified Helmholtz Coil system. The proposed arrangement of three pairs of Helmholtz Coils placed will be placed along the three orthogonal directions. A pair of Helmholtz Coils is separated by the value of their shared radius. The Biot-Savart Law for calculating the magnetic field at a point along the axis of a loop of wire is shown in Eq. (21):

$$B = \frac{\mu_0 IR^2}{2(R^2 + a^2)^{3/2}} \quad (21)$$

defined by two coils placed in series. These two coils have the same radius and current magnitude/direction and are represented by this equation,  $\mu_0$  is the magnetic permeability of free space,  $I$  is the coil current,  $R$  is the radius of the coil, and  $a$  is the distance between the coil and the point at which the measurement is taken, which can be anywhere along the coil axis. From this equation, an equation can be derived to calculate the magnetic field for a pair of coils, Helmholtz coils. This is Eq. (22):

$$B = \frac{\mu_0 (NIR^2)}{2(R^2 + (R/2)^2)^{3/2}} \quad (22)$$

Here the total current,  $I$ , is calculated from the current supplied to a coil and the number of turns of wire for a coil,  $N$ . The coils are separated by a distance equal to the radius of the coils,  $R$ . The point at which the measurement is taken,  $a$  is half of the radius,  $R/2$ . The two coils are in series with the same current direction so that the magnetic fields generated by the two are additive. Each coil is the same with respect to all the quantities of interest, the entire equation describing one coil can be multiplied by two. Simplifying Eq. (3), results in Eq. (4):

$$B = (4/5)^{3/2} \frac{\mu_0 NI}{R} \quad (23)$$

Equation (21) can be used to calculate the magnetic field obtained from a pair of true Helmholtz Coils—where the coils are separated by their shared radius. However, to account for the fact that each pair of coils will instead be separated by their diameter rather than their radius for the reasons discussed above, Eq. (24) is derived from Eq. (21) where  $a$  now represents half the diameter of the coils or the radius,  $R$ .

$$B = \frac{\mu_0 (NIR^2)}{2(R^2 + R^2)^{3/2}} \quad (24)$$

Simplifying this equation results in Eq. (25):

$$B = (1/2)^{3/2} \frac{\mu_0 NI}{R} \quad (25)$$

Equation (25) is the equation that ultimately describes each pair of coils in one direction for the coil system designed within this thesis. The magnetic field generated by each pair of coils along their shared axis can be determined when the number of turns, current, and radius are specified. Alternately, this equation can be rearranged to solve for a different unknown; for example, it will be useful to solve for the number of turns of wire needed to achieve a desired magnetic field value. It can be seen that the numerical constant in Eq. (25), describing what will be referred to as the modified pair of Helmholtz Coils, is smaller than the constant that appears in Eq. (23), which describes the true pair of Helmholtz Coils. This is to be expected, as separating the coils by a larger distance and measuring the magnetic field at a further point from the two sources generating the field should reduce the measured field. The result of this solution will require a greater number of wire turns for a given current. Also an increase supplied current to generate a given field value in the modified coil system could be used, more than would be required by the true Helmholtz Coil system. The consequence of this fact will require a greater number of wire turns or more current supplied to generate a given field value in the modified coil system than would be required by the true Helmholtz Coil system. There are many calibration techniques that have been developed for magnetometers utilizing different methods. An example of a physical method is the swinging compass procedure, which has long found use in sea navigation. This process requires that the magnetic field values be recorded using the ship's compass for the eight cardinal directions and these values are then compared with reference values to obtain the offset in measurements [26]. Generally, this method is two-dimensional and not very precise and so will not be suitable when working with a three-axis magnetometer in this application. For compensating the external hard and soft error sources, which once again take the form of an ellipsoid shape rather than sphere that is offset from the origin, numerical methods using matrices

are commonly employed and are considered to be the simpler and less accurate linear approach. In this approach, it is sought to do away with this mathematical approach in compensating for these errors. Helmholtz coils have found use in compensating the internal biasing errors of magnetometers. With regards to the tri-axis design, existing designs tend to attempt to hold true to the requirement that the separation between the coils be their shared radius, which again requires that the design allow for the intersection and overlap of coils, making the realization of the actual system more complex [27]. Here, the design to be explored keeps the coil system design simple to realize by separating the coils by their diameter instead.

Once it was determined that the test system for the magnetometers would be of a modified Helmholtz design for all three axes, the specifics of the design were laid out. Originally, the limiting factors of the design were to be that a total magnetic field capable of being generated by the system was to be about 6 G—as that was the limit of the range of one of the magnetometers to be tested with the system. In addition, the current was originally limited to 5A and was therefore the value used in the initial calculations. The reason for this was to plan for the event in which there would be difficulties in obtaining six power supplies with a higher current rating. The physical coil system was to be assembled using six aluminum bicycle rims with a diameter of 16.5 in. (radius of 8.25 in.), each wrapped with 16 gauge insulated copper wire. Before continuing, vector relationship equations must be employed to determine the required magnetic field that must be generated for each of the three axes, such that the resultant magnetic field vector has a magnitude of roughly 6 G through the center of the system. A magnetic field vector of 3 G along each of the x, y, and z axes will give a resultant vector magnitude of 5.20 G through the center of the system.

Now, if Eq. (25) is employed and rearranged to solve for  $N$ , the number of windings of copper wire needed for each of the bicycle rims can be estimated given the requirement that for each pair, about 3 G of magnetic field be generated when 5A of current is supplied to each pair. This equation predicts that roughly 28 windings are necessary for each of the six bicycle rim coils.

In order to better visualize the magnetic fields predicted to be generated by the entire tri-axis coil system, the software package COMSOL was used to simulate the coil system design using the Magnetic Fields package. From within the COMSOL model, the six aluminum rims, the current to be supplied to the coils, the number of wrappings of copper wire, etc. could all be specified. The final simulation results are shown in Fig. 23 which shows an individual slice of the three dimensional simulation. Figure 24 shows the complete three dimensional model results. Similar to the calculated scenario, this simulation specified an 8.25 in. radius for the coils, a current of 5A supplied to each pair of coils and 28 wrappings for each of the coils. It can be seen that at the very center of the assembly about 5.5 G is the predicted value of the magnetic field according to the color legend. This does compare very closely with the vector magnitude of 5.20 G and direction through the center of the system that was calculated above.

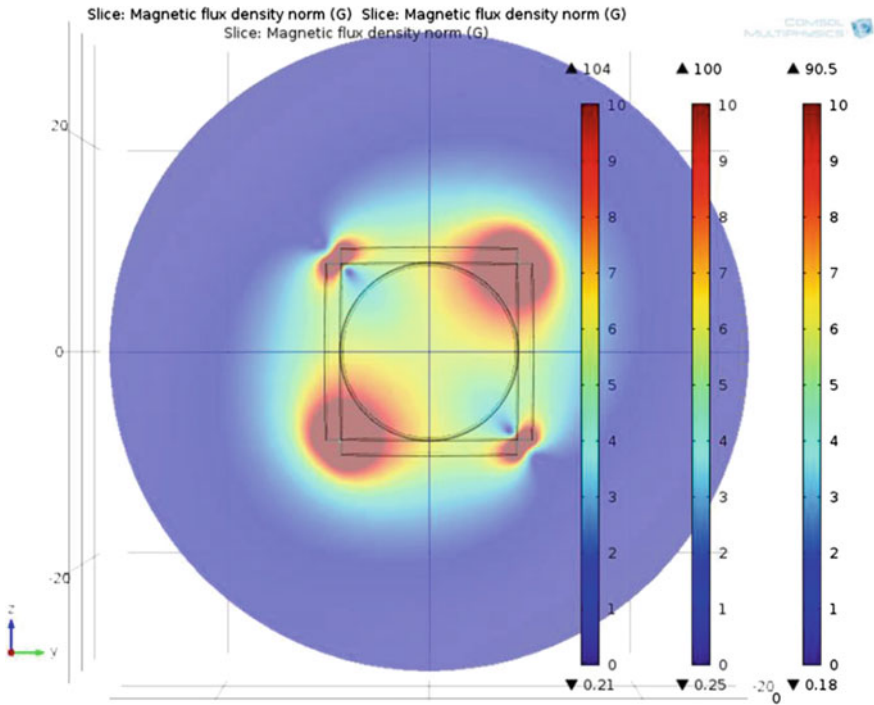


**Fig. 23** One-dimension of the Comsol model of the three-axis Helmholtz coil test system

It should be noted that for this modified Helmholtz Coil design, the COMSOL model shows that the fields within the system are not as uniform as what would be expected from the true Helmholtz Coil design.

It can be seen in Fig. 23 that there are various “hot spots” near adjacent coils that create an overall less than uniform pattern of the magnetic field in the system. Regardless, the center point of the system, where the magnetometer will be placed, shows a “sweet spot” for the field which Eq. (6) can predict fairly accurately. Using the results of the COMSOL simulation, the six bicycle rims were hand wrapped with 28 turns of the copper wire with the goal of achieving the roughly 6 G of magnetic field at center of the physical assembly. Figure 25 shows the actual physical assembly of the coil system. The base of the assembly seen in this figure is also constructed of aluminum, chosen like the bicycle rims for its non-magnetic properties and hence, not a source of magnetic distortion to the system. Finally, the rod extending to the center of the system from a three axis manipulator located to the left of the system is also aluminum and this is where the magnetometer will be placed. Each coil was wrapped twice, with 28 turns going in the clockwise (CW) direction and another 28 turns counterclockwise (CCW) (Fig. 25).

For the three pairs of coils for the x, y, and z direction, each wrapped in the clockwise and counterclockwise direction, a total of six power supplies were



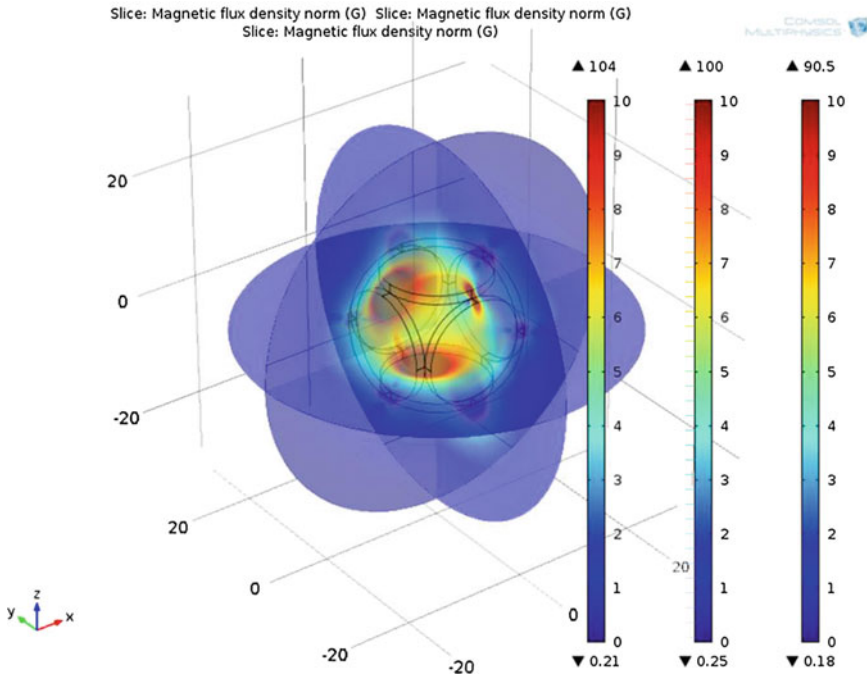
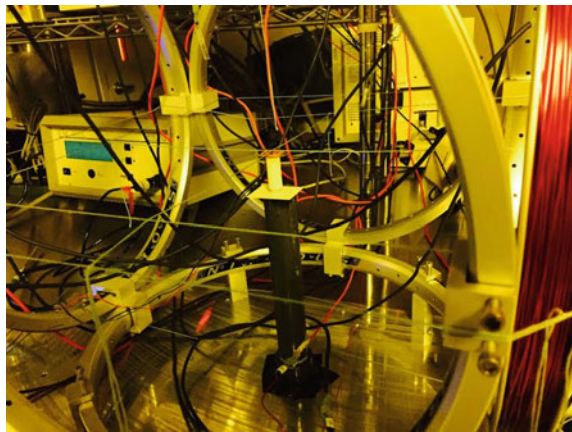


Fig. 24 Full three dimensional model of the three-axis Helmholtz test system

Fig. 25 Modified 3-axes Helmholtz Coil design. The strings were used to help square the sensor in the test area

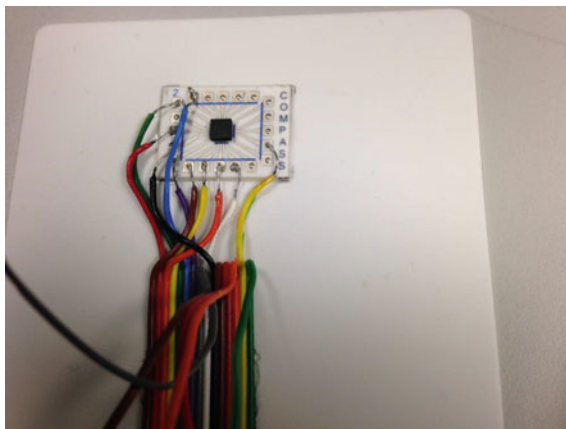


needed for the assembly. This setup is useful in the absence of switching power supplies, because to otherwise switch the direction of the current, the leads would have to manually be switched between the CW and CCW sets of wrappings and checked each time for accuracy. Also, with two directions of wrappings, there exists the possibility of running both sets of coils at the same time with different currents

supplied to the two sets, if an offset value of magnetic field needs to be generated by the second set to adjust the overall magnetic field for the system. Two Honeywell chips, the HMC5843 and HMC5883L were considered for use in testing the coil system. The HMC5843 chips were already available for use and provided the opportunity to construct a hybrid circuit, while the HMC5883L breakout boards were purchased fully assembled. These two chips were very similar in design and operation. The HMC5883L was designed to be the successor to the HMC5843 and boasted a few improvements, including a smaller size, less connections, the ability to measure a larger range of fields, etc.

The HMC5843 chip was explored first. The chip itself has dimensions of  $4\text{ mm} \times 4\text{ mm} \times 1\text{ mm}$  with 20 pads, each with a width of 0.25 mm (about 10 mils) and spacing between the pads of 0.25 mm. Using AutoCAD, a layout for the design of a hybrid circuit was constructed. The design was simple, requiring only that there be conducting traces from the chip pad to larger printed pads at the edges of the alumina substrate for the purposes of making external connections to the chip. An additional AutoCAD layer was specified for printing a dielectric layer onto the substrate to function as a solder dam to prevent leeching of solder applied to the conducting pads out to the traces. Figure 26 shows the completed hybrid circuit with the HMC5843 chip soldered to the printed circuit and wired to the connector. Wires soldered to the magnetometer were then fed outside of the coil system an Arduino Nano placed at the base of manipulator. The magnetometer is a slave device with a unique hardware address and must be connected to a master that can supply the power, clock, collect the data, etc. The Arduino was then connected by way of an USB to a computer which ultimately supplied the power to the Arduino. It also ran the Arduino IDE with code uploaded to the Nano that collected the magnetic fields data along the x, y, and z axes and calculated the overall vector magnitude and angles. The results of testing the physical coil assembly and magnetometer with the Arduino code when 5A of current was supplied to each of the three pairs of coils. It can be seen that the x and y axis values are in agreement with

**Fig. 26** HMC5843 hybrid circuit with external connections



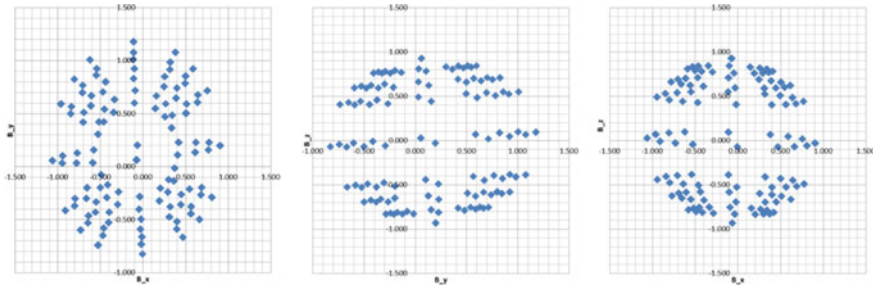


**Fig. 27** Plot of the corrected output of the HMC5883L magnetometer in x-z, y-z, and x-y with various offset currents to compensate the Earth's field. Centered, spherical magnetic field data with an offset current applied in the z coil set

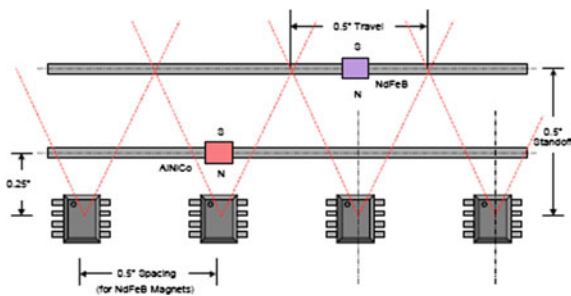
Eq. (25), which once again, predicts 3 G of field under these conditions. The discrepancy is mainly with the z axis measurement, as it showed the greatest variation from 3 G, with roughly 2 G of magnetic field. And, it was this measurement that reduced the magnitude of the resultant field to 4.748 G. Recall that the mathematical prediction was 5.20 G while the COMSOL model predicted 5.5 G. The fact that the experimental model resulted in a total magnetic field value significantly different from both the COMSOL model and the mathematical calculations would be expected, as the latter two are considered more ideal or simplistic than the real world situation in which the experimental model operates. Real world conditions include the presence of Earth's magnetic field along with many other potential sources of stray magnetic fields—the surrounding power supplies, computers, etc. in the lab are just a few examples.

The following graphs show the results of using the HMC5883L chip to find sources of magnetic field distortion (Fig. 27).

## 6 Commercial Devices

Commercial sensing opportunities for AMR magnetometers are broken into two basic areas. The first of these is for feedback for process control systems and the second use generally for safety equipment. Automotive sensors are usually used for engine control as well as safety equipment. The feedback control applications are often position sensing and can be very similar to automotive applications, but many are static position devices. These static position devices often set the range of motion for robotic and automatic equipment. A common commercial device is the meander sensor. Meander sensors can be used to measure anything from ring-magnets to high-current fields generated by power lines.

**Fig. 28** Honeywell's HMC1501 array. The outputs can be compared to determine position of the sliding magnets, from Honeywell Application Notes [28]



## 6.1 Discrete Devices

Common uses for the discrete AMR devices often are low field applications. The low field applications are mostly compass applications but some applications like linear position sensors may use an array of discrete sensors. An example of an array of position sensors is shown in Fig. 28.

This arrangement of sensors can be used with either multi-channel analog to digital converters and computer algorithms or can be used with a series of amplifiers and comparators in a purely analog circuit.

## 6.2 Automotive Applications (Monolithic IC)

In the early 1970s a small group of engineers began a revolution in automotive sensing using magnetic sensors. These individuals perceived that magnetic sensing could replace the mechanical points in the automotive ignition system. By that time optical ignition systems had been used in automotive racing, but these systems proved unreliable in field testing due to their tendency to perform poorly in less than ideal conditions. A team at Honeywell's MicroSwitch Division saw that the Hall Effect sensor along with a vane could replace the cam and points in an automotive ignition system. This team installed this first solid state vane switch in a 1960s Ford Mustang and drove into the future. This first introduction of a point-free magnetic sensor based ignition system open the door to computerized automotive control systems. These developments allowed the automotive manufacturers to reduce emissions of primary pollutants. Modern engine control systems now monitor intake air, crank position, cam position, and exhaust gases. In the early 1990s, automotive manufacturers were looking to meet more stringent emissions criteria. The criteria were essentially no misfire during start-up, and no fuel tank vapor leaks. To improve the quality of the signal and to simplify the control system by removing unneeded components the spark distributor was replaced by the gear-tooth sensor. It was in this environment that the first automotive grade anisotropic magnetoresistive sensor [29, 30] was introduced. This sensor is a

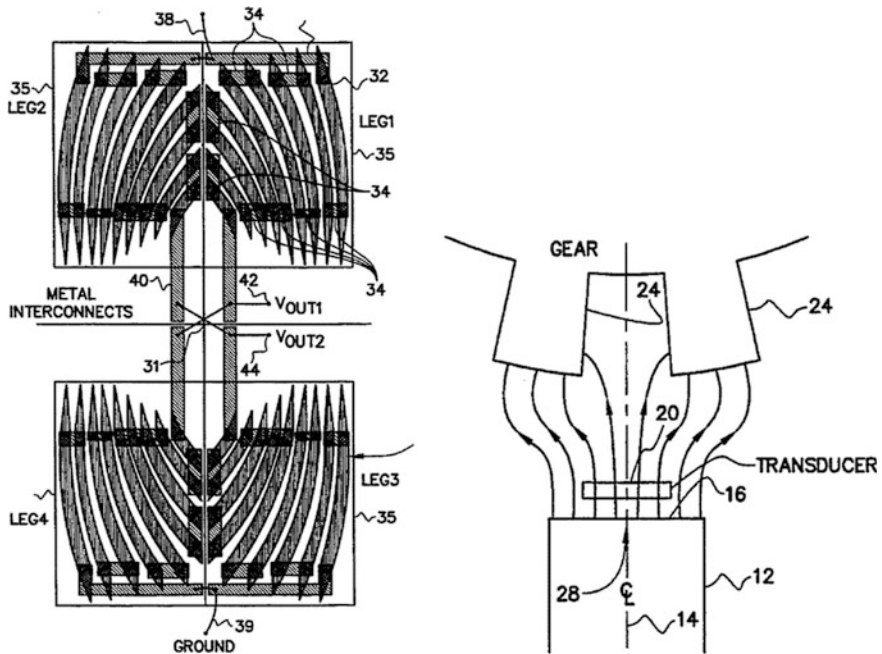
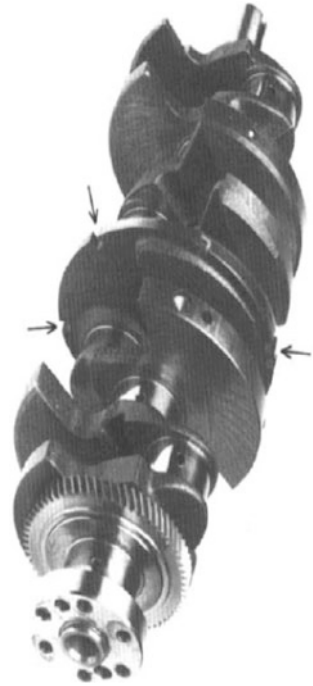


**Fig. 29** First automotive grade gear tooth AMR sensor element. This sensor element in combination with the process patent created a monolithic sensor that could withstand 185 °C ambient [29, 30]

monolithic sensor—monolithic means that the sensor and the circuitry exists on the same chip and is shown in Fig. 29. Previous AMR monolithic sensors (high current sensors) produced by the Honeywell team were limited by process technology to 85 °C, these sensors have now been replaced by newer technology. Previous AMR monolithic sensors (high current sensors) produced by the Honeywell team were limited by process technology to 85 °C, these sensors have now been replaced by newer technology. The Hall Effect sensor, which is still used by the majority of automotive platforms, requires that the direction of the field be oriented out of plane. The Hall Effect sensor is mounted in such a way that the sensor is essentially sitting on top of the magnet and the gear tooth sensor passes just short of the sensor surface. Figure 30 shows an automotive crankshaft with target from the early 1990s. The problem with this sensor configuration is that the gap spacing is the distance between the surface of the Hall sEffect sensor and the magnetic target and is dependent on the over-molding, fit and engine wear. The form of the waveform coming off of the gear-tooth is roughly sinusoidal with an dc offset. When a Hall Effect sensor is placed close to a gear-tooth it produces a high dc offset and a high amplitude waveform. As the spacing opens up, the offset reduces and the peak-to-peak values reduce significantly. To maximize the sensors usefulness, the Hall Effect sensor electronics require a partial rotation of the gear-tooth target to

**Fig. 30** Early 1990s crankshaft with target. The arrows show the target [31]



calibrate the sensor. This causes excess unburned hydrocarbons to be released in the atmosphere during start-up.

On the other hand, the Anisotropic MagnetoResistor (AMR) sensor depends on the in-plane magnetic fields. The AMR sensor is sensitive to the ratio of the in-plane fields which can be quite consistent over several millimeters. This consistency and high signal to noise ratio makes the AMR sensor quite desirable for start-up conditions. Unlike the Hall Effect sensor, the circuitry used for the AMR sensor can be relatively simple temperature compensated dc operational amplifier (Hall Effect sensors can also be dc but the gap spacing is significantly smaller, as much as 25–50 %). The AMR sensor can be near zero-speed at start-up, which means that the sensor can detect the first gear-tooth transition. The AMR sensor can be used with an encoded target rather than a gear-tooth target. The encoded target can be found in U.S. Manufactured vehicles built by General Motors after 1997 (C5 Corvette). Other automotive applications in which AMR sensors can be used are as follows, wheel-speed, gear-shift, automatic transmission sensing, and compass applications. In the early days of AMR automotive sensing, there was a concern for stray fields effecting the AMR sensors. This was allayed by a group of Honeywell design engineers who surveyed all the possible sources of stray fields in the greater Chicago area.



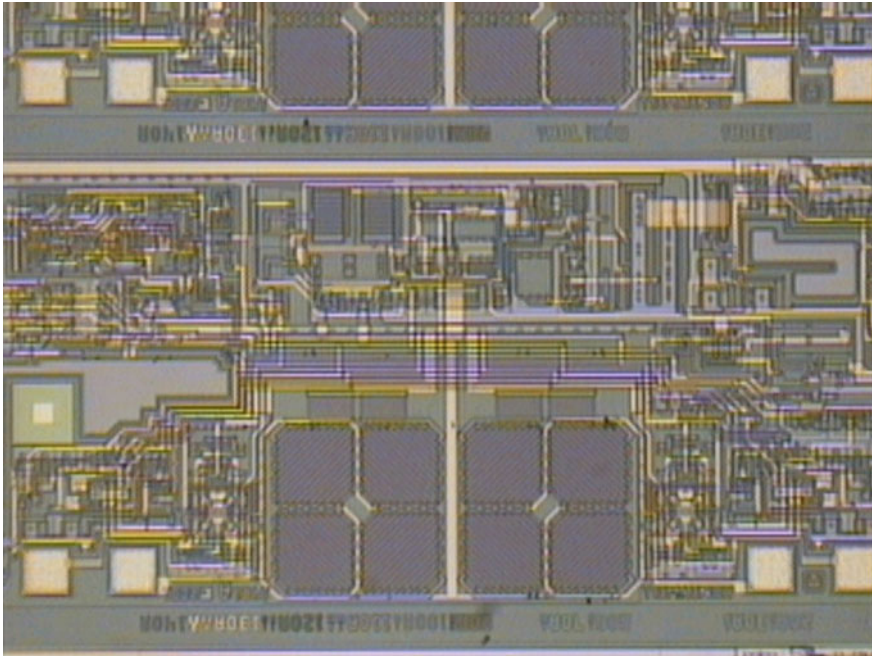


**Fig. 31** Prototype speed and direction sensor manufactured by Honeywell’s MicroSwitch Division in the early 2000s. The monolithic device is made from ion-milled permalloy and double level metal. The sensors are  $\pm 45^\circ$  meander sensors. The logic family is I2L. *Photo care of Author*

The stray fields were discovered to be much less than the fields needed to cause a significant error in the sensor. Figure 31 shows a prototype permalloy speed [32] and direction sensor built by Honeywell’s Microswitch Division. This device has two separate permalloy sensors spaced far enough apart to create a phase shift. This phase shift along with simple digital logic allows the device to detect direction along with rotational speed for a ring magnet. The application envisioned for this device was an anti-lock brake sensor that could a car from rolling backwards on a steep hill.

## 7 Advances in AMR Magnetometry

The bulk of work in AMR magnetometry over the last 15 years has focused on improving modeling of AMR sensors. A significant amount of work has been performed to analyze permalloy nanowires and nanodots. Recent work by Corte-León et al. [33] looks at the effect of pinning at the corners of 150 nm structures. They noted that even these nanostructures magnetic response is still dominated by the AMR effect while they were studying how to determine the best

way to analyze magnetization reversal. The effect of aspect ratio is studied by Singh and Mandel [34] along with temperature effects. Spin-waves in permalloy nanostructures are studied by Nguyen et al. [35] using high frequency measurement techniques with good correlation of theory for experimental. Many new papers are studying these physical properties of nanowires, but this has not been translated to the area practical magnetometry. Most modern advances in AMR magnetometry has been in the commercial sphere and can be found during cursory searches on patent agencies. A recent advancement on the planer hall device was filed with the U.S. Patent and Trademark Office by Klien et al. [36] and a modification of the dual track automotive sensor was filed by Pant and Lakshman [37]. Significant work still needs to be done in trying to characterize the three dimensional tensor that represents the magnetoresistor also connecting that to the basic mechanisms. Nanoscale work is showing that even though the resistors are getting smaller, the AMR effect may exist at a very fundamental level.

**Acknowledgments** The Authors would like to thank the many fine engineers, technicians and production operators at Honeywell's Sensor Fab in Richardson, Texas for helping collect reams of data on the behavior of permalloy from 1994 to 2002. We would also like to thank Misty Haji-Sheikh for patiently editing this work. Additionally, like the lead author, many of the people have moved on to other careers such Bob Biard (Honeywell Retired), Wayne Kilian, Ron Foster, and John Schwartz (Honeywell Retired), but all have had a part in this work in some way or another.

## References

1. W. Thompson, On the electro-dynamic qualities of metal: effects of magnetization on the electric conductivity of nickel and of iron. *Proceedings of the Royal Society of London*, vol. 8, (1897), pp. 546–550
2. T.R. McGuire, R.I. Potter, Anisotropic magnetization in ferromagnetic 3d alloys. *IEEE Trans. Magn.* **MAG-11**(4), 1018–1037 (1975)
3. L.I. Maissel, R. Glang, *Handbook of Thin Film Technology* (McGraw-Hill Handbooks, New York City, 1970)
4. B.B. Pant. Magnetoresistive sensors. *Sci. Honeyweller* **8**(1), 29–34 (1987)
5. Y. Lee, A.R. Koymen, M.J. Haji-Sheikh, Discovery of cross-tie walls at saw-tooth magnetic domain boundaries in permalloy films. *Appl. Phys. Lett.* **72**(7), 851–852 (1998)
6. A. Garcia-Arribas, E. Fernández, A.V. Svalov, G.V. Kurylanskaya, A. Barrainkua, D. Navas, J.M. Barandiaran, Tailoring the magnetic anisotropy of thin film permalloy microstrips by combined shape and induced anisotropies. *Euro. Phys. J. B* **86**(4), 136 (2013)
7. J.P. Heremans, Magnetic field sensors for magnetic position sensing in automotive applications (invited review). *Mat. Res. Soc. Symp. Proc.* **1**, 63–74 (1997)
8. S. Tumanski, *Thin Film Magnetoresistive Sensors* (IOP, Bristol, U.K., 2001)
9. E.H. Hall, On a new action of the magnet on electric currents. *Am. J. Math.* **2**(3), 287–292 (1879)
10. R.R. Birss, *Symmetry and Magnetism* (North Holland, Amsterdam, The Netherlands, 1964)
11. E.C. Stoner, E.P. Wohlfarth, A mechanism of magnetic hysteresis in heterogeneous alloys. *Philos. Trans. R. Soc. A: Phys. Math. Eng. Sci.* **240**(826), 599–642 (1948)
12. D.A. Thompson, L.T. Romankiew, A.F. Mayadas, Thin film resistors in memory, storage and related applications. *IEEE Trans. Magn.* **MAG-11**(4), 1039–1050 (1975)



13. C.P. Batterel, M. Galinier, Optimization of the planer hall effect in ferromagnetic thin films for device design. *IEEE Trans. Magn.* **MAG-5**(1), 18–28 (1969)
14. C.-R. Chang, A hysteresis model for planar hall effect in the films. *IEEE Trans. Magn.* **36**(4), 1214–1217 (2000)
15. M.J. Haji-Sheikh, G. Morales, B. Altuncevahir, A.R. Koymen, Anisotropic magnetoresistive model for saturated sensor elements. *Sens. J. IEEE* **5**(6), 1258–1263
16. J.F. Nye, *Physical Properties of Crystals: Their Representation by Tensors and Matrices* (Oxford University Press, Oxford, 1985)
17. S. Chikazumi, S.H. Charap, *Physics of Magnetism* (Krieger Pub Co, Malabar, 1978)
18. T. Tanaka, K. Yazawa, H. Masuya, Structure, magnetization reversal, and magnetic anisotropy of evaporated cobalt films with high coercivity. *IEEE Trans. Magn.* **MAG-21**(5), 2090–2096 (1985)
19. J.A. Baldwin Jr., G.M. Pickles. Power spectrum of Barkhausen noise in simple materials. *J. Appl. Phys.* **43**(11), 4746–4749 (1972)
20. B.B. Pant, Effect of interstrip gap on the sensitivity of high sensitivity magnetoresistive transducer. *J. Appl. Phys.* **79**, 6123 (1996)
21. C.A. Grimes, P.L. Trouilloud, L. Chun, Switchable lossey/non-lossey permalloy thin films. *IEEE Trans. Magn.* **33**(5), 3996–3998 (1997)
22. R. Mathias, J. McCord, K. Ramstöck, D. Berkov, Formation and annihilation of edge walls in thin-film permalloy stripes. *IEEE Trans. Magn.* **33**(5), 3993–3995 (1997)
23. H. Zhang, C. Li, R. Divan, A. Hoffmann, P. Wang, Broadband mag-noise of patterned permalloy thin films. *IEEE Trans. Magn.* **46**(6), 2442–2445 (2010)
24. E.D. van Hattum, D.B. Boltje, A. Palmero, W.M. Arnoldbik, H. Rudolph, F.H.P.M. Habraken, On the argon and oxygen incorporation into SiO<sub>x</sub> through ion implantation during reactive plasma magnetron sputter deposition. *Appl. Surf. Sci.* **255**, 3079–3084 (2008)
25. S.C. Mukhopadhyay, Y.-M.R. Huang, *Sensors: Advancements in Modeling, Design Issues, Fabrication and Practical Applications*, 1st edn. (Springer, Berlin, 2008)
26. N. Bowditch, *The American Practical Navigator: An Epitome of Navigation* (National Imagery and Mapping Agency, Bethesda, 2002)
27. HCS1: Helmholtz Coil System. HCS1 product datasheet, Barrington Instruments
28. Honeywell's Application Notes, Applications of Magnetic Position Sensors
29. M.J. Haji-Sheikh, TaN/NiFe/TaN Anisotropic Magnetic Sensor Element. Patent Number 5,667,879, 16 Sept 1997
30. D.R. Krahn, Magnetoresistive proximity sensor. U.S. Patent 5,351,028 A
31. J. Heremans, Solid state magnetic field sensors and applications. *J. Phys. D Appl. Phys.* **26**, 1149–1168 (1993)
32. M. Haji-Sheikh, M. Plagens, R. Kryzanowski, Magnetoresistive speed and direction sensing method and apparatus. U. S. Patent Number 6,784,659
33. H. Corte-León, V. Nabaei, A. Manzin, J. Fletcher, P. Krzysteczko, H.W. Schumacher, O. Kazakova, Anisotropic magnetoresistance state space of permalloy nanowires with domain wall pinning geometry. *Sci. Rep.* **4**(6045) (2014) doi:[10.1038/srep06045](https://doi.org/10.1038/srep06045)
34. A.K. Singh, K. Mandal, Effect of aspect ratio and temperature on magnetic properties of permalloy nanowires. *J. Nanosci. Nanotechnol.* **14**(7), 5036–5041 (2014)
35. T.M. Nguyen, M.G. Cottam, H.Y. Liu, Z.K. Wang, S.C. Ng, M.H. Kuok, D.J. Lockwood, K. Nielsch, U. Gösele, Spin waves in permalloy nanowires: the importance of easy-plane anisotropy. *Phys. Rev. B* **73**, 140402(R) (2006)
36. L. Klein, A. Grosz, M.O.R. Vladislav, E. Paperno, S. Amrusi, I. Faivinov, M. Schultz, O. Sinwani, High resolution planar hall effect sensors. Patent Application US 20140247043 A1
37. B.B. Pant, L. Withanawasam, Anisotropic magneto-resistance (amr) gradiometer/magnetometer to read a magnetic track. Patent Application US 20130334311 A1